# Three-Port Small Signal Admittance-Based Model of VSCs for Studies of Multi-terminal HVDC Hybrid AC/DC Transmission Grids

J. Pedra, *Member IEEE,* L. Sainz, and Ll. Monjo

***Abstract*- Multi-terminal high voltage direct current (HVDC) systems, together with AC transmission systems and voltage source converters (VSCs), form hybrid AC/DC grids with complex dynamic and transient interactions. VSCs characterization taking into account DC- and AC-side dynamics in order to study these interactions is not yet well solved. This paper presents a three-port transfer admittance-based matrix model of VSCs that can be applied for such purpose. It is derived from *dq*-complex space vectors and characterizes both AC- and DC-side dynamics by relating AC- and DC-side current and voltages in a three-dimensional admittance transfer matrix which considers the VSC outer control loops. The paper also proposes a systematical procedure for studying multi-terminal HVDC hybrid AC/DC transmission grids by the Norton admittance method, where the proposed VSC model can be easily included in the Norton admittance matrix. This procedure allows the study of grid dynamics using impedance-based stability criteria. The proposed model and procedure are applied to a stability study in a multi-terminal HVDC hybrid AC/DC transmission grid. PSCAD/EMTDC simulations are used to validate the application.**

***Index Terms*— Impedance modeling, voltage source converters, HVDC transmission.**

## I. Introduction

Multi-Terminal high voltage direct current (HVDC) systems have emerged as a promising power transmission technology because of their ability to increase power transfer capability and improve power system operation flexibility and energy source interconnection. These HVDC systems are linked to AC transmission grids by means of line commutated converters (LCCs), voltage source converters (VSCs) and modular multilevel converters (MMCs), building hybrid AC/DC grids with complex dynamic and transient interactions [1], [2]. Novel phenomena such as oscillatory instabilities appear in hybrid AC/DC systems with VSCs and MMCs [2]. However, their assessment, prediction and solution have not yet been well studied. State space [3], [4] and frequency domain [5] – [11] methods are common approaches for analyzing instability phenomena in these systems [12] – [15]. Frequency domain methods based on the impedance-based characterization of power systems are also widely used to assess system stability because they can be applied from either analytical models or measurements and with less computing effort than the state space method [14], [15].

The AC- and DC-side admittance-based models of VSCs are typically studied separately to include the VSC admittance transfer function in AC- and DC-side stability studies, respectively. These AC- and DC-side admittance-based models are derived from *dq*-real transfer function-based [5], [8] – [10], [12] – [15], *dq*-complex transfer function-based [16], [17] and phasor-based [18] methods. DC-side admittance-based models of VSCs considering AC-side dynamics have recently been published [12], [13]. The *dq*-complex approach is becoming a powerful tool for VSC admittance modeling because it can be used to systematically determine and program VSC admittance-based models, as well as to characterize sequence-component coupling and mirror frequency effect dynamics [7], [19], [20]. This is also studied in [19], [21], where the modified sequence-domain (MSD) impedance matrix model is proposed on the basis of the Park (*dq*-real) and Ku (*dq*-complex) transformations [22], [23]. The above methods are widely applied to single VSC systems, but only a few works analyze stability in large-scale AC and DC systems composed of multiple VSCs [15], [24], [25]. The admittance matrix approach is used in these studies as it provides a simple and accurate way to characterize large-scale power system behavior in frequency domain. Recently, a worthy AC-side stability study of multi-terminal VSC power systems based on the nodal admittance matrix approach and the AC-side 2x2 input admittance-based matrix of VSCs has been presented in [26].

Hybrid AC/DC grid issues cannot be studied when AC- and DC-side dynamics are modeled separately, as in the above references. Moreover, although AC- and DC-side dynamics could be included in these models, the AC-side admittance-based model is a two-port model that only relates AC-side voltages and currents, and the DC-side admittance-based model is a single port model that only relates DC-side voltages and currents. A three-port transfer admittance-based

This work was supported in part by the Ministerio de Ciencia, Innovación y Universidades under Grant RTI2018-095720-B-C33 and in part by the Ministerio de Economía, Inndustria y Competitividad and the EU FEDER Funds under Grant DPI2017-84503-R.

J. Pedra and L. Sainz are with the Dep. of Elect. Eng., UPC, Av. Diagonal 647, 08028 Barcelona, Spain (mails: pedra@ee.upc.edu, sainz@e.upc.edu). Ll. Monjo is with the Dep. of Industrial and Design System Eng., Univ. Jaume I, Av. de Vicent Sos Baynat, s/n, 12071 Castelló de la Plana, Spain (mail: lmonjo@uji.es).

matrix model of VSCs relating AC- and DC-side voltages and currents is necessary to study hybrid AC/DC HVDC grids from the nodal admittance matrix approach. There are multi-terminal HVDC hybrid AC/DC transmission grids which cannot be reduced to the AC or DC side and must be studied from the three-port transfer admittance-based matrix model of VSCs and the nodal admittance matrix of the hybrid grid to assess stability. A *dq*-real [27], [28] and $\alpha\beta$-domain [29] three-port equivalent circuits of VSCs considering AC- and DC-side dynamics are presented in the literature. However, these equivalent circuits take into account the VSC modulation function only. These equivalent circuits are used to derive the AC-side admittance matrix model of VSCs considering the phase-locked loop (PLL), VSC time delay and current control [27], and to derive a block diagram of the closed-loop small signal model for VSCs including AC- and DC-side dynamics and considering the direct-voltage control loop, PLL, VSC time delay and current control [28], [29]. Additionally, the AC-side admittance matrix model of VSCs [28], [29] and the 1x2 gain matrix that relates AC- and DC-side voltages [29] are derived from the block diagram. Three-port transfer admittance-based matrix models that consider AC and DC dynamics and can be applied in hybrid AC/DC grid studies have recently been presented [14], [18], [20]. However, they neither consider all VSC control blocks nor are applied to multi-terminal HVDC hybrid AC/DC transmission grids. In [14], an MSD three-port AC/DC admittance-based model is presented. This model considers the $P-Q$, $V_{dc}-Q$ and $V-f$ operation modes of VSCs but does not include the grid voltage feedforward low-pass filter of the VSC current control loop and the VSC time delay. The grid voltage feedforward low-pass filter bandwidth and VSC time delay are the main parameters to achieve VSC passivity at harmonic frequencies [9]. The grid voltage feedforward low-pass filter bandwidth also affects the VSC non-passivity region caused by outer control loops at near-synchronous frequencies [9], [10]. The non-consideration of these parameters in the three-port AC/DC admittance-based model is a drawback to characterizing the VSC negative-damping region, which defines near-synchronous and harmonic stability conditions [9], [10]. A simple AC/DC coupled system is analyzed by Kirchhoff laws in order to study the properties and impacts of impedance rotation on the AC/DC coupled system in [14] but no general methodology for assessing multi-terminal HVDC hybrid AC/DC transmission grid stability based on the three-port AC/DC admittance-based model is provided. The Norton admittance methodology is used for comparing different stability criteria but this methodology is applied to an AC interconnected system with VSCs where DC-side dynamics are not considered, i.e., no three-port AC/DC admittance-based model is used in this study. In [18], the three-port AC/DC matrix is modeled in *dq*, sequence and phasor domains by considering only the inner current controller and the PLL. A simple VSC HVDC link with an impedance connected at the AC or DC side is analyzed. The VSC AC- and DC-side impedance model is also derived from the three-port matrix. In [20], the proposed three-port VSC model only considers the direct-voltage control loop and is only applied to study the stability of a point-to-point HVDC transmission system from the control block diagram of the AC- and DC-side system. As far as the authors know, stability of large-scale hybrid VSC-HVDC grids has not yet been studied on the basis of three-port transfer admittance-based matrix of VSCs and the nodal admittance matrix approach.

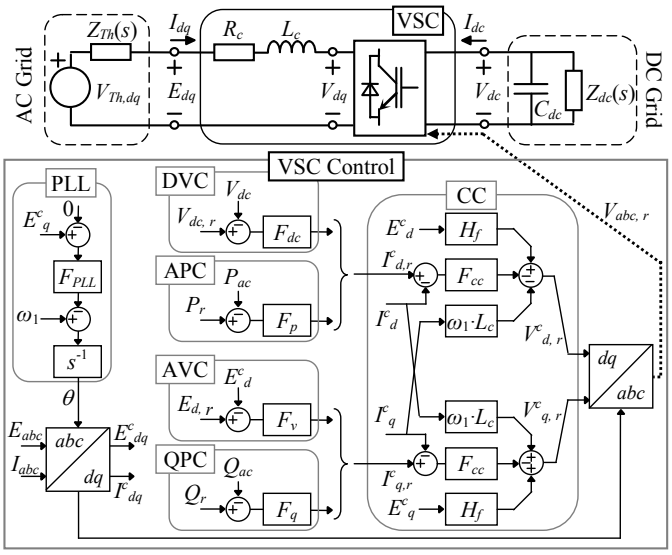


Fig. 1. Grid-connected VSC circuit.

This paper presents a novel VSC three-port admittance-based model using *dq*-complex space vectors for multi-terminal VSC-HVDC hybrid AC/DC transmission grid studies. The model extends systematically and rigorously the three-port transfer admittance-based matrix models in [14], [18] and [20] by considering the grid voltage feedforward, VSC time delay and main outer control loops (including the control loops of the operation modes $V_{dc}-E_{ac}$ and $P-E_{ac}$). Moreover, the VSC AC- and DC-side impedance models are derived from the three-port matrix model. The paper also extends the Norton admittance method used for AC-side stability analysis of multi-terminal VSC power systems in [26] to study AC- and DC-side stability of multi-terminal HVDC hybrid AC/DC transmission grids, where the proposed three-port admittance matrix model is easily included in the nodal admittance matrix of large-scale hybrid AC/DC grids handling VSCs as independent components. This methodology allows the assessment of multi-terminal HVDC hybrid AC/DC transmission grid stability using impedance-based stability criteria (e.g., Generalized Nyquist Criterion, GNC). Stability issues in a multi-terminal HVDC hybrid AC/DC grid are studied to show the paper's contribution. The results obtained are validated with PSCAD/EMTDC simulations.

## II. Three-Port Grid-connected VSC System Modeling

The three-port small signal admittance-based model of the grid-connected VSC in Fig. 1 is derived in this Section [9], [10], [14]. The VSC control is represented by the inner current controller (CC) and the following outer control loops:

alternating-power control (APC), direct-voltage control (DVC), reactive-power control (QPC) and alternating-voltage control (AVC). These outer control loops make it possible to characterize the main VSC operation modes (i.e., modes $P-Q$, $V_{dc}-Q$, $V_{dc}-E_{ac}$ and $P-E_{ac}$) [9], [10]. The PLL is also considered in the control modeling, and the superscript "c" denotes the converter *dq*-domain. No super index is used on the grid *dq*-domain variables for simplicity. All the VSC admittance-based models in this Section are numerically validated but this is not shown for space reasons.

Complex transfer functions (see Appendix A) are used to model grid-connected VSCs with *dq*-complex space vectors from the *dq*-real small signal impedance model [16], [17] and obtain the three-port small signal admittance-based model. The *dq*-real small signal impedance model of VSCs is summarized in Appendix B to follow clearly the three-port small signal admittance-based model in the next Subsections.

### A. AC grid relation

According to (30) and (32), the voltage balance across the converter $R_c-L_c$ filter is expressed with *dq*-complex space vectors as

$$\begin{bmatrix}\Delta\mathbf{E_{dq}}\\ \Delta\mathbf{E}^{*}_{\mathbf{dq}}\end{bmatrix}=\begin{bmatrix}\mathbf{Z}^{+}_{\mathbf{c}} & \mathbf{Z}^{-}_{\mathbf{c}}\\ (\mathbf{Z}^{-}_{\mathbf{c}})^{*} & (\mathbf{Z}^{+}_{\mathbf{c}})^{*}\end{bmatrix}\begin{bmatrix}\Delta\mathbf{I_{dq}}\\ \Delta\mathbf{I}^{*}_{\mathbf{dq}}\end{bmatrix}+\begin{bmatrix}\Delta\mathbf{V_{dq}}\\ \Delta\mathbf{V}^{*}_{\mathbf{dq}}\end{bmatrix} \quad (1)$$
$$\Rightarrow\quad \Delta\mathbf{E}^{\mathbf{m}}_{\mathbf{dq}}=\mathbf{Z}^{\pm}_{\mathbf{c}}\Delta\mathbf{I}^{\mathbf{m}}_{\mathbf{dq}}+\Delta\mathbf{V}^{\mathbf{m}}_{\mathbf{dq}},$$

where $\mathbf{E_{dq}}=(E_d+jE_q)/\sqrt{2}$, $\mathbf{V_{dq}}=(V_d+jV_q)/\sqrt{2}$, $\mathbf{I_{dq}}=(I_d+jI_q)/\sqrt{2}$, $\mathbf{Z}^{+}_{\mathbf{c}}=R_c+L_c(s+j\omega_1)$, $(\mathbf{Z}^{+}_{\mathbf{c}})^{*}=R_c+L_c(s-j\omega_1)$, $\mathbf{Z}^{-}_{\mathbf{c}}=0$ and $\omega_1=2\pi f_1$ is the fundamental angular frequency of the grid.

### B. AC-DC converter relations

According to (33), the VSC output voltage $V_{dq}$ can be related to the DC voltage $V_{dc}$ by using the modulation function $m_{dq}=[m_d\ m_q]^{\mathrm{T}}$ and *dq*-complex space vectors (30) as the small signal relation

$$\begin{bmatrix}\Delta\mathbf{V_{dq}}\\ \Delta\mathbf{V}^{*}_{\mathbf{dq}}\end{bmatrix}=\begin{bmatrix}\Delta\mathbf{m_{dq}}\\ \Delta\mathbf{m}^{*}_{\mathbf{dq}}\end{bmatrix}V_{dc0}+\begin{bmatrix}\mathbf{m_{dq0}}\\ \mathbf{m}^{*}_{\mathbf{dq0}}\end{bmatrix}\Delta V_{dc} \quad (2)$$
$$\Rightarrow\quad \Delta\mathbf{V}^{\mathbf{m}}_{\mathbf{dq}}=\Delta\mathbf{m}^{\mathbf{m}}_{\mathbf{dq}}V_{dc0}+\mathbf{m}^{\mathbf{m}}_{\mathbf{dq0}}\Delta V_{dc},$$

where $\mathbf{m_{dq}}=(m_d+jm_q)/\sqrt{2}$ and $V_{dc0}$ and $\mathbf{m_{dq0}}$ are the steady-state operating points of the DC voltage and the modulation function, respectively.

According to (35), the small signal relation between the DC current $I_{dc}$ and the AC current can be expressed by using the *dq*-complex space vectors (30) as the small signal relation

$$\Delta I_{dc}=-\begin{bmatrix}\mathbf{m}^{*}_{\mathbf{dq0}} & \mathbf{m_{dq0}}\end{bmatrix}\begin{bmatrix}\Delta\mathbf{I_{dq}}\\ \Delta\mathbf{I}^{*}_{\mathbf{dq}}\end{bmatrix}-\begin{bmatrix}\mathbf{I}^{*}_{\mathbf{dq0}} & \mathbf{I_{dq0}}\end{bmatrix}\begin{bmatrix}\Delta\mathbf{m_{dq}}\\ \Delta\mathbf{m}^{*}_{\mathbf{dq}}\end{bmatrix} \quad (3)$$
$$\Rightarrow\quad \Delta I_{dc}=-(\mathbf{m}^{\mathbf{m}}_{\mathbf{dq0}})^{H}\Delta\mathbf{I}^{\mathbf{m}}_{\mathbf{dq}}-(\mathbf{I}^{\mathbf{m}}_{\mathbf{dq0}})^{H}\Delta\mathbf{m}^{\mathbf{m}}_{\mathbf{dq}},$$

where the superscript $H$ indicates the transpose and complex conjugate (Hermitian conjugate). Note that the three-phase set of modulation functions $\{m_a, m_b, m_c\}=M\{\cos(\omega_1 t+\phi_m),\cos(\omega_1 t+\phi_m-2\pi/3),\cos(\omega_1 t+\phi_m+2\pi/3)\}$ is transformed into the *dq*-complex space vector $\mathbf{m_{dq}}=(\sqrt{3}/2)M\angle\phi_m$ by applying the normalized Ku (*dq*-complex) transformation [16], [22], [23].

### C. PLL relations

The AC current, AC voltage and modulation function in the converter and grid *dq*-domains (36) can be expressed with *dq*-complex space vectors from the following small signal relations obtained by applying the complex transfer functions (30):

$$\begin{aligned}&\Delta\mathbf{I}^{\mathbf{cm}}_{\mathbf{dq}}=\Delta\mathbf{I}^{\mathbf{m}}_{\mathbf{dq}}+\mathbf{G}^{\pm}_{\mathbf{pIIi}}\Delta\mathbf{E}^{\mathbf{m}}_{\mathbf{dq}}\\ &\mathbf{G}^{+}_{\mathbf{pIIi}}=-\mathbf{G}^{-}_{\mathbf{pIIi}}=-G_{pll}(s)(I_{d0}+jI_{q0})/2,\end{aligned} \quad (4)$$

$$\begin{aligned}&\Delta\mathbf{E}^{\mathbf{cm}}_{\mathbf{dq}}=\mathbf{G}^{\pm}_{\mathbf{pIIv}}\Delta\mathbf{E}^{\mathbf{m}}_{\mathbf{dq}}\\ &\mathbf{G}^{+}_{\mathbf{pIIv}}=1-G_{pll}(s)(E_{d0}+jE_{q0})/2\\ &\mathbf{G}^{-}_{\mathbf{pIIv}}=1-\mathbf{G}^{+}_{\mathbf{pIIv}},\end{aligned} \quad (5)$$

$$\begin{aligned}&\Delta\mathbf{m}^{\mathbf{cm}}_{\mathbf{dq}}=\Delta\mathbf{m}^{\mathbf{m}}_{\mathbf{dq}}+\mathbf{G}^{\pm}_{\mathbf{pIIm}}\Delta\mathbf{E}^{\mathbf{m}}_{\mathbf{dq}},\\ &\mathbf{G}^{+}_{\mathbf{pIIm}}=-\mathbf{G}^{-}_{\mathbf{pIIm}}=-G_{pll}(s)(m_{d0}+jm_{q0})/2,\end{aligned} \quad (6)$$

where $G_{PLL}(s)=F_{PLL}(s)/(s+E_{d0}F_{PLL}(s))$ and $F_{PLL}(s)$ is the transfer function of the PLL control (see (36) in Appendix B). Note that the *dq*-complex space vectors in the converter *dq*-domain have the superscript "c" whereas no super index is used on the grid *dq*-domain variables.

### D. Inner CC loop relations

The control law of the inner CC loop (37) is expressed with *dq*-complex space vectors (30) as

$$\Delta\mathbf{V}^{\mathbf{cm}}_{\mathbf{dq,r}}=-\mathbf{F}^{\pm}_{\mathbf{cc}}(\Delta\mathbf{I}^{\mathbf{cm}}_{\mathbf{dq,r}}-\Delta\mathbf{I}^{\mathbf{cm}}_{\mathbf{dq}})-\mathbf{Z}^{\pm}_{\boldsymbol{\omega}}\Delta\mathbf{I}^{\mathbf{cm}}_{\mathbf{dq}}+\mathbf{H}^{\pm}_{\mathbf{f}}\Delta\mathbf{E}^{\mathbf{cm}}_{\mathbf{dq}}, \quad (7)$$

where $\mathbf{F}^{+}_{\mathbf{cc}}=D(s)F_{cc}(s)$, $\mathbf{Z}^{+}_{\boldsymbol{\omega}}=D(s)\cdot jL_c\omega_1$, $\mathbf{H}^{+}_{\mathbf{f}}=D(s)H_f(s)$, $\mathbf{F}^{-}_{\mathbf{cc}}=\mathbf{Z}^{-}_{\boldsymbol{\omega}}=\mathbf{H}^{-}_{\mathbf{f}}=0$ and $F_{cc}(s)$, $D(s)$ and $H_f(s)$ are the transfer function of the CC, VSC time delay and grid voltage feedforward low-pass filter (see (37) in Appendix B). According to (33), the *dq*-complex space vector of the VSC reference voltage is expressed as $\boldsymbol{\Delta}\mathbf{V}^{\mathbf{cm}}_{\mathbf{dq,r}}=V_{dc0}\boldsymbol{\Delta}\mathbf{m}^{\mathbf{cm}}_{\mathbf{dq}}$.

### E. Outer control loop relations

The reference currents generated by the outer control loops can be related to the DC voltage and the AC voltage and current at the PCC with *dq*-complex space vectors as the following general expression:

$$\Delta\mathbf{I}^{\mathbf{cm}}_{\mathbf{dq,r}}=-\mathbf{F}^{\mathbf{m}}_{\mathbf{o}}\Delta V_{dc}-\mathbf{G}^{\pm}_{\mathbf{o}}\Delta\mathbf{I}^{\mathbf{cm}}_{\mathbf{dq}}-\mathbf{Y}^{\pm}_{\mathbf{o}}\Delta\mathbf{E}^{\mathbf{cm}}_{\mathbf{dq}}, \quad (8)$$

where the complex transfer matrices $\mathbf{F}^{\mathbf{m}}_{\mathbf{o}}$, $\mathbf{G}^{\pm}_{\mathbf{o}}$ and $\mathbf{Y}^{\pm}_{\mathbf{o}}$ depend on the VSC outer control loops (see Appendix B).

### F. Link between inner, PLL and outer control loop relations

The following relation is obtained by substituting the outer control loop law (8) and the PLL relations (4), (5) and (6) in

the control law of the inner current control loop (7):

$$\Delta \mathbf{m}^{\mathbf{m}}_{\mathbf{dq}} = \frac{1}{V_{dc0}}\left\{\mathbf{F}^{\pm}_{\mathbf{cc}}\mathbf{F}^{\mathbf{m}}_{\mathbf{o}}\Delta V_{dc} + (\mathbf{Z}^{\pm}_{\mathbf{pi}} + \mathbf{F}^{\pm}_{\mathbf{cc}}\mathbf{G}^{\pm}_{\mathbf{o}})\Delta \mathbf{I}^{\mathbf{m}}_{\mathbf{dq}} + \mathbf{H}^{\pm}_{\mathbf{o}}\Delta \mathbf{E}^{\mathbf{m}}_{\mathbf{dq}}\right\}, \quad (9)$$

where

$$\begin{aligned}\mathbf{H}^{\pm}_{\mathbf{o}} &= (\mathbf{Z}^{\pm}_{\mathbf{pi}} + \mathbf{F}^{\pm}_{\mathbf{cc}}\mathbf{G}^{\pm}_{\mathbf{o}})\mathbf{G}^{\pm}_{\mathbf{plli}} + (\mathbf{H}^{\pm}_{\mathbf{f}} + \mathbf{F}^{\pm}_{\mathbf{cc}}\mathbf{Y}^{\pm}_{\mathbf{o}})\mathbf{G}^{\pm}_{\mathbf{pllv}} - V_{dc0}\mathbf{G}^{\pm}_{\mathbf{pllm}} \\ \mathbf{Z}^{\mathbf{m}}_{\mathbf{pi}\pm} &= \mathbf{F}^{\pm}_{\mathbf{cc}} - \mathbf{Z}^{\pm}_{\boldsymbol{\omega}}.\end{aligned} \quad (10)$$

*G. Three-port small signal admittance-based model*

The DC voltage is related to the AC voltage and current at the PCC by substituting (9) and (1) in (2):

$$\begin{aligned}&\mathbf{A}_{\mathbf{v}}\Delta V_{dc} = \mathbf{B}_{\mathbf{v}}\Delta \mathbf{I}^{\mathbf{m}}_{\mathbf{dq}} + \mathbf{C}_{\mathbf{v}}\Delta \mathbf{E}^{\mathbf{m}}_{\mathbf{dq}} \\ &\mathbf{A}_{\mathbf{v}} = \mathbf{m}^{\mathbf{m}}_{\mathbf{dq0}} + \mathbf{F}^{\pm}_{\mathbf{cc}}\mathbf{F}^{\mathbf{m}}_{\mathbf{o}} \qquad \mathbf{B}_{\mathbf{v}} = -\mathbf{Z}^{\pm}_{\mathbf{c}} - \mathbf{Z}^{\pm}_{\mathbf{pi}} - \mathbf{F}^{\pm}_{\mathbf{cc}}\mathbf{G}^{\pm}_{\mathbf{o}} \\ &\mathbf{C}_{\mathbf{v}} = \mathbf{I}_2 - \mathbf{H}^{\pm}_{\mathbf{o}},\end{aligned} \quad (11)$$

where $\mathbf{I_2}$ = diag(1, 1) is the 2x2 identity matrix.

The DC current is related to the DC voltage and the AC voltage and current at the PCC by substituting (9) in (3):

$$\begin{aligned}&\Delta I_{dc} = A_i\Delta V_{dc} + \mathbf{B_i}\Delta \mathbf{I}^{\mathbf{m}}_{\mathbf{dq}} + \mathbf{C_i}\Delta \mathbf{E}^{\mathbf{m}}_{\mathbf{dq}} \\ &A_i = -\frac{1}{V_{dc0}}(\mathbf{I}^{\mathbf{m}}_{\mathbf{dq0}})^H\mathbf{F}^{\pm}_{\mathbf{cc}}\mathbf{F}^{\mathbf{m}}_{\mathbf{o}} \quad \mathbf{C_i} = -\frac{1}{V_{dc0}}(\mathbf{I}^{\mathbf{m}}_{\mathbf{dq0}})^H\mathbf{H}^{\pm}_{\mathbf{o}} \\ &\mathbf{B_i} = -(\mathbf{m}^{\mathbf{m}}_{\mathbf{dq0}})^H - \frac{1}{V_{dc0}}(\mathbf{I}^{\mathbf{m}}_{\mathbf{dq0}})^H(\mathbf{Z}^{\pm}_{\mathbf{pi}} + \mathbf{F}^{\pm}_{\mathbf{cc}}\mathbf{G}^{\pm}_{\mathbf{o}}).\end{aligned} \quad (12)$$

The relations between voltages and currents can be directly obtained from (11) and (12):

$$\begin{aligned}\Delta I_{dc} &= (A_i + \mathbf{B_i}\mathbf{B}_{\mathbf{v}}^{-1}\mathbf{A}_{\mathbf{v}})\Delta V_{dc} + (\mathbf{C_i} - \mathbf{B_i}\mathbf{B}_{\mathbf{v}}^{-1}\mathbf{C}_{\mathbf{v}})\Delta \mathbf{E}^{\mathbf{m}}_{\mathbf{dq}} \\ \Delta \mathbf{I}^{\mathbf{m}}_{\mathbf{dq}} &= \mathbf{B}_{\mathbf{v}}^{-1}\mathbf{A}_{\mathbf{v}}\Delta V_{dc} - \mathbf{B}_{\mathbf{v}}^{-1}\mathbf{C}_{\mathbf{v}}\Delta \mathbf{E}^{\mathbf{m}}_{\mathbf{dq}}.\end{aligned} \quad (13)$$

Considering that $\Delta \mathbf{I}^{\mathbf{m}}{}_{\mathbf{dq}} = [\Delta \mathbf{I}_{\mathbf{dq}}\ \Delta \mathbf{I}^{*}{}_{\mathbf{dq}}]^{\mathrm{T}}$ and $\Delta \mathbf{E}^{\mathbf{m}}{}_{\mathbf{dq}} = [\Delta \mathbf{E}_{\mathbf{dq}}\ \Delta \mathbf{E}^{*}{}_{\mathbf{dq}}]^{\mathrm{T}}$, (13) characterizes the three-port small signal admittance matrix of VSCs, as follows:

$$\begin{bmatrix}\Delta I_{dc}\\ \Delta \mathbf{I}_{\mathbf{dq}}\\ \Delta \mathbf{I}^{*}_{\mathbf{dq}}\end{bmatrix} = \underbrace{\begin{bmatrix}Y_{cc} & \mathbf{Y_{cp}} & \mathbf{Y_{cn}}\\ \mathbf{Y_{pc}} & \mathbf{Y_{pp}} & \mathbf{Y_{pn}}\\ \mathbf{Y_{nc}} & \mathbf{Y_{np}} & \mathbf{Y_{nn}}\end{bmatrix}}_{\mathbf{Y}^{(\mathbf{AC/DC})}(s)}\begin{bmatrix}\Delta V_{dc}\\ \Delta \mathbf{E}_{\mathbf{dq}}\\ \Delta \mathbf{E}^{*}_{\mathbf{dq}}\end{bmatrix}$$

$$Y_{cc} = A_i + \mathbf{B_i}\mathbf{B}_{\mathbf{v}}^{-1}\mathbf{A}_{\mathbf{v}} \quad \underbrace{\begin{bmatrix}\mathbf{Y_{cp}} & \mathbf{Y_{cn}}\end{bmatrix}}_{\mathbf{Y_{12}}} = \mathbf{C_i} - \mathbf{B_i}\mathbf{B}_{\mathbf{v}}^{-1}\mathbf{C}_{\mathbf{v}} \quad (14)$$

$$\underbrace{\begin{bmatrix}\mathbf{Y_{pc}}\\ \mathbf{Y_{nc}}\end{bmatrix}}_{\mathbf{Y_{21}}} = \mathbf{B}_{\mathbf{v}}^{-1}\mathbf{A}_{\mathbf{v}}\Delta V_{dc} \quad \underbrace{\begin{bmatrix}\mathbf{Y_{pp}} & \mathbf{Y_{pn}}\\ \mathbf{Y_{np}} & \mathbf{Y_{nn}}\end{bmatrix}}_{\mathbf{Y_{22}}} = -\mathbf{B}_{\mathbf{v}}^{-1}\mathbf{C}_{\mathbf{v}}.$$

According to [14], the non-consideration of the grid voltage feedforward low-pass filter $H_f(s)$ or VSC time delay leads to $D(s) = H_f(s) = 1$ in (7) and simplifies the three-port small signal admittance-based model (14). However, these assumptions could also lead to inaccurate assessment of near-synchronous and harmonic instabilities [9], [10].

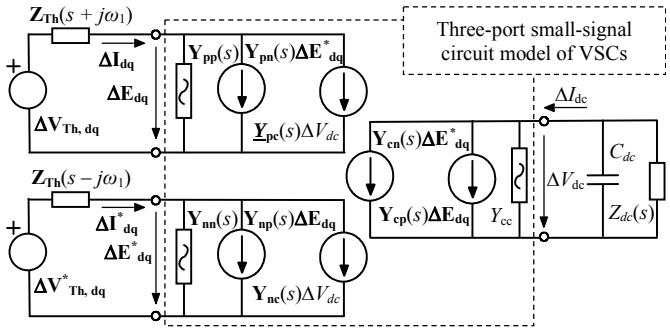


Fig. 2. Three-port small signal circuit model of VScs.

Fig. 2 shows the three-port small signal circuit model of VSCs derived from (14).

*H. AC- and DC-side small signal admittance-based model*

The VSC AC- and DC-side equivalent admittance models can be easily derived from (14). The AC-side equivalent admittance $\mathbf{Y}^{(\mathbf{AC})}(s)$ is obtained by imposing in (14) the DC-side relation $\Delta I_{dc} = -Y_{Edc}\Delta V_{dc}$:

$$\begin{bmatrix}-Y_{Edc}\Delta V_{dc}\\ \Delta \mathbf{I}^{\mathbf{m}}_{\mathbf{dq}}\end{bmatrix} = \begin{bmatrix}Y_{cc} & \mathbf{Y_{12}}\\ \mathbf{Y_{21}} & \mathbf{Y_{22}}\end{bmatrix}\begin{bmatrix}\Delta V_{dc}\\ \Delta \mathbf{E}^{\mathbf{m}}_{\mathbf{dq}}\end{bmatrix} \Rightarrow \Delta \mathbf{I}^{\mathbf{m}}_{\mathbf{dq}} = \mathbf{Y}^{(\mathbf{AC})}(s)\Delta \mathbf{E}^{\mathbf{m}}_{\mathbf{dq}} \quad (15)$$

$$\mathbf{Y}^{(\mathbf{AC})}(s) = \mathbf{Y_{22}} - \mathbf{Y_{21}}(Y_{Edc} + Y_{cc})^{-1}\mathbf{Y_{12}}.$$

The DC-side equivalent admittance $Y^{(\mathrm{DC})}(s)$ is obtained by imposing in (14) the following AC-side relation:

$$\begin{bmatrix}\Delta \mathbf{I_{dq}}\\ \Delta \mathbf{I^*_{dq}}\end{bmatrix} = -\underbrace{\begin{bmatrix}\mathbf{Y^+_{Th}} & \mathbf{Y^-_{Th}}\\ (\mathbf{Y^-_{Th}})^* & (\mathbf{Y^+_{Th}})^*\end{bmatrix}}_{\mathbf{Y^{\pm}_{Th}}}\begin{bmatrix}\Delta \mathbf{E_{dq}}\\ \Delta \mathbf{E^*_{dq}}\end{bmatrix}. \quad (16)$$

The DC-side equivalent admittance is expressed as

$$\begin{bmatrix}\Delta I_{dc}\\ -\mathbf{Y^{\pm}_{Th}}\Delta \mathbf{E}^{\mathbf{m}}_{\mathbf{dq}}\end{bmatrix} = \begin{bmatrix}Y_{cc} & \mathbf{Y_{12}}\\ \mathbf{Y_{21}} & \mathbf{Y_{22}}\end{bmatrix}\begin{bmatrix}\Delta V_{dc}\\ \Delta \mathbf{E}^{\mathbf{m}}_{\mathbf{dq}}\end{bmatrix} \Rightarrow \quad (17)$$

$$\Delta I_{dc} = Y^{(\mathrm{DC})}(s)\Delta V_{dc} \quad Y^{(\mathrm{DC})}(s) = Y_{cc} - \mathbf{Y_{12}}(\mathbf{Y^{\pm}_{Th}} + \mathbf{Y_{22}})^{-1}\mathbf{Y_{21}}.$$

*I. Three-port small signal admittance-based model validation*

The circuit in Fig. 3(a) and the data in Table I are used to numerically validate the three-port small signal admittance-based model (14) in Fig. 3(b), where the DC-side equivalent impedance $Z^{(\mathrm{DC})}(s) = 1/Y^{(\mathrm{DC})}(s)$ (17) is compared to PSCAD/EMTDC simulations. The DC-side test is the simplest procedure to validate the three-port small signal admittance matrix because the determination of all the terms in this matrix is avoided (note that $Y^{(\mathrm{DC})}(s)$ (17) is derived from the three-port small signal admittance-based model (14)). The AC grid is characterized by an AC voltage source in series with an $R_{ac}-L_{ac}$ impedance and a shunt capacitor $C_f$ connected to the VSC terminals (see Fig. 3(a)). The VSC operates in mode $V_{dc}-Q$. In the PSCAD/EMTDC simulations, a series perturbation of voltage $V_{dc}$ at frequency $f$ is applied on the DC side of the VSC while the 50 Hz AC-side voltage source is a short-circuit at frequency $f$. The DC-side consumed current $I_{dc}$ is determined from the Fast Fourier Transform (FFT) of the

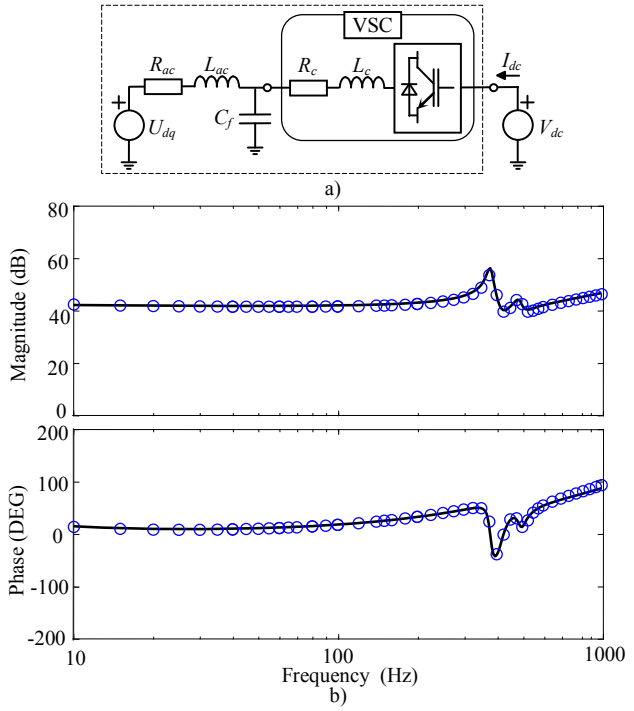


Fig. 3. DC test for model validation: a) Test circuit. b) DC-side equivalent impedance $Z^{(DC)}(s) = 1/\ Y^{(DC)}(s)$ [Lines: (17). Circles: PSCAD/EMTDC simulations].

PSCAD/EMTDC simulation currents when they reach the steady state. Subsequently, the value of the DC-side equivalent impedance is calculated from the previous results as $Z^{(DC)}(s) = V_{dc}/I_{dc}$ and is represented versus frequency $f$ (circles in Fig. 3(b)). The accurate results provided by the model are highlighted. Similar results are obtained with the other VSC operation modes.

According to the circuit in Fig. 4(a) and the data in Table I, the three-port small signal admittance-based model (14) is also validated in Fig. 4(b), where the AC-side equivalent admittance matrix $\mathbf{Y}^{(AC)}(s)$ (15) is compared to PSCAD/EMTDC simulations.

TABLE I
MODEL VALIDATION DATA
BASE VALUES: $U_{B,\,AC}$ = 220 KV, $U_{B,\,DC}$ = 440 KV, $S_B$ = 1000 MVA

| | Parameters | Data |
|---|---|---|
| AC grid | $R_{ac}$, $L_{ac}$ | 0.0025 pu, 0.05 pu |
| AC filter | $C_f$ | 0.304 pu |
| DC load | $R_{dc}$, $L_{dc}$ | 0.00051 pu, 0.0032 pu |
| DC filter | $C_{dc}$ | 1.824 pu |
| VSC data | $P_{vsc,\,N}$, $V_{dc,\,0}$ | 1000 MW, 440 kV |
| VSC control | $f_s$, $T_d$, $\alpha_f$ | 2 kHz, 0.3 ms, 106.8 rad/s |
| | $R_c$, $L_c$ | 0.025 pu, 0.25 pu |
| | $k_{p,cc}$ , $k_{i,cc}$ | 1 pu, 0.031 pu |
| | $k_{p,pll}$, $k_{i,pll}$ | 0.48 pu, 0.031pu |
| | $k_{p,dc}$, $k_{i,dc}$ | 0.15 pu, 0.058 pu |
| | $k_{p,\,p}$, $k_{i,p}$ | 0.15 pu, 0.058 pu |

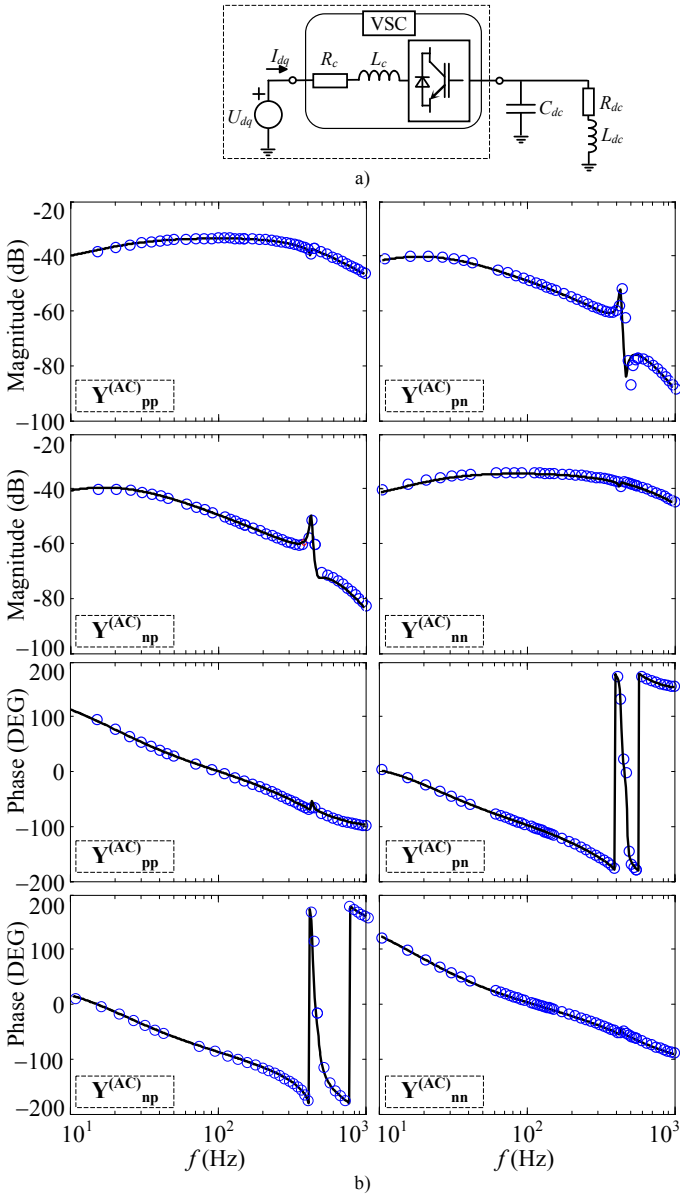


Fig. 4. AC test for model validation: a) Test circuit. b) AC-side equivalent admittances $\mathbf{Y}^{(AC)}(s)$ [Lines: (15). Circles: PSCAD/EMTDC simulations].

## III. STABILITY OF HVDC HYBRID AC/DC GRIDS

The circuit of Fig. 5 shows the schematic diagram of multi-terminal HVDC transmission grids linked to AC transmission grids by VSCs. The incremental symbol Δ of the small signal variables is omitted for the sake of simplicity. The multi-terminal HVDC hybrid AC/DC transmission grid (i. e., AC and HVDC transmission grids) is characterized by its admittance matrix $\mathbf{Y_G}(s)$ and the different components connected at the AC and DC grid buses which are represented by their equivalent circuits.

The AC grid components are the following:

- AC grids characterized by the current balance at their Norton equivalent circuit buses:

$$\underbrace{\begin{bmatrix}\mathbf{I_{dq}}\\ \mathbf{I^{*}_{dq}}\end{bmatrix}_{i}}_{\mathbf{I}_i^{(AC)}} = \underbrace{\begin{bmatrix}\mathbf{I_{dq}}\\ \mathbf{I^{*}_{dq}}\end{bmatrix}_{\mathbf{g},i}}_{\mathbf{I}_{\mathbf{g},i}^{(AC)}} - \underbrace{\begin{bmatrix}\mathbf{Z_g^{+}} & \mathbf{Z_g^{-}}\\ (\mathbf{Z_g^{-}})^{*} & (\mathbf{Z_g^{+}})^{*}\end{bmatrix}_{i}^{-1}}_{\mathbf{Y}_i^{(AC)}} \underbrace{\begin{bmatrix}\mathbf{V_{dq}}\\ \mathbf{V^{*}_{dq}}\end{bmatrix}_{i}}_{\mathbf{V}_i^{(AC)}} \quad (i=1,\ldots a), \quad (18)$$

where $\mathbf{Z}^{+}_{\mathbf{g}}(s) = R_g + L_g(s + j\omega_1)$ and $\mathbf{Z}^{-}_{\mathbf{g}} = 0$ [16].

- AC loads characterized by their *dq*-complex admittance matrix $\mathbf{Y_i}^{(AC)}(s)$ ($i = 1, \ldots b$). These loads can be the impedance loads whose admittance matrix is obtained from their *dq*-real admittance matrix and transformation (30) or VSC applications (e.g., in distributed generation), whose admittance matrix is derived from the models (38) and (2) in [9] and [10], respectively, and transformation (30).
- Terminals without any connected external components represented as open-circuit buses characterized by zero values of the current source and admittance of the Norton equivalent circuit, i.e., $\mathbf{I_i}^{(AC)} = \mathbf{0}_{2x1}$ and $\mathbf{Y_i}^{(AC)} = \mathbf{0}_{2x2}$ ($i = 1, \ldots c$).

The DC grid components are the following:

- DC grids characterized by the current balance at their Norton equivalent circuit buses:

$$I_i^{(DC)} = I_{g,i}^{(DC)} - Y_i^{(DC)}(s)V_i^{(DC)} \quad (i=1,\ldots d). \quad (19)$$

- DC loads characterized by their admittance transfer function $Y_i^{(DC)}(s)$ ($i = 1, \ldots e$).
- Terminals without any connected external components represented as open-circuit buses characterized by zero values of the current source and admittance of the Norton equivalent circuit, $I_i^{(AC)} = Y_i^{(AC)} = 0$ ($i = 1, \ldots g$).

Note that the VSCs are modeled by their three-port small signal admittance matrix $\mathbf{Y}_i^{(AC/DC)}(s)$ ($i = 1, \ldots h$) in (14). VSC models are locally evaluated in the *dq*- reference frame of each VSC and a matrix rotation is required to refer all of them to the same *dq*-global or common reference frame, which can be arbitrarily chosen [14].

System stability is commonly assessed by applying frequency domain methods such as the Nyquist stability criterion to the impedance ratio of the source and load equivalent systems (i.e., to the loop transfer function $L(s) = Z_{source}(s)\cdot Y_{load}(s)$) partitioned at some point of the studied grid. However, it must be borne in mind that this criterion is a local stability approach sensitive to system partitions, which can lead to inaccurate stability predictions [14]. If and only if the impedance ratio $Z_{source}(s)\cdot Y_{load}(s)$ does not have any right-half-plane (RHP) poles, stability of the closed loop system can be assessed by encirclements of $Z_{source}(s)\cdot Y_{load}(s)$ in clockwise direction around the –1 point. Otherwise, the number of RHP poles of $Z_{source}(s)\cdot Y_{load}(s)$ must also be considered. Commonly, these RHP poles are not assessed in frequency domain studies and the encirclements of $Z_{source}(s)\cdot Y_{load}(s)$ are only checked when the Nyquist stability criterion is applied. According to this, the criterion fails when the source or the load equivalent systems are unstable (i.e., when $Z_{source}(s)$ or $Y_{load}(s)$ have RHP poles). This instability can occur when the source and load equivalent systems come from a grid with VSCs due to the interaction between the VSC controls and the passive components of the grid [14]. To avoid the above issue and according to [26], system stability is assessed by considering the whole system without any partition.

Considering the rotation issue of VSC frames addressed, the relations between voltages and currents at the multi-terminal HVDC hybrid AC/DC transmission grid are expressed as

$$\left.\begin{aligned}\mathbf{i} &= \mathbf{Y_G}(s)\mathbf{v}\\ \mathbf{i} &= \mathbf{i_E} - \mathbf{Y_E}(s)\mathbf{v}\end{aligned}\right\} \Rightarrow \mathbf{v} = \left(\mathbf{Y_G}(s) + \mathbf{Y_E}(s)\right)^{-1}\mathbf{i_E}, \quad (20)$$

where $\mathbf{Y_G}(s)$ is admittance matrix of the multi-terminal HVDC hybrid AC/DC transmission grid. The voltage $\mathbf{v}$ at the grid terminals and the current source $\mathbf{i_E}$ and the equivalent admittance $\mathbf{Y_E}(s)$ of the external components are

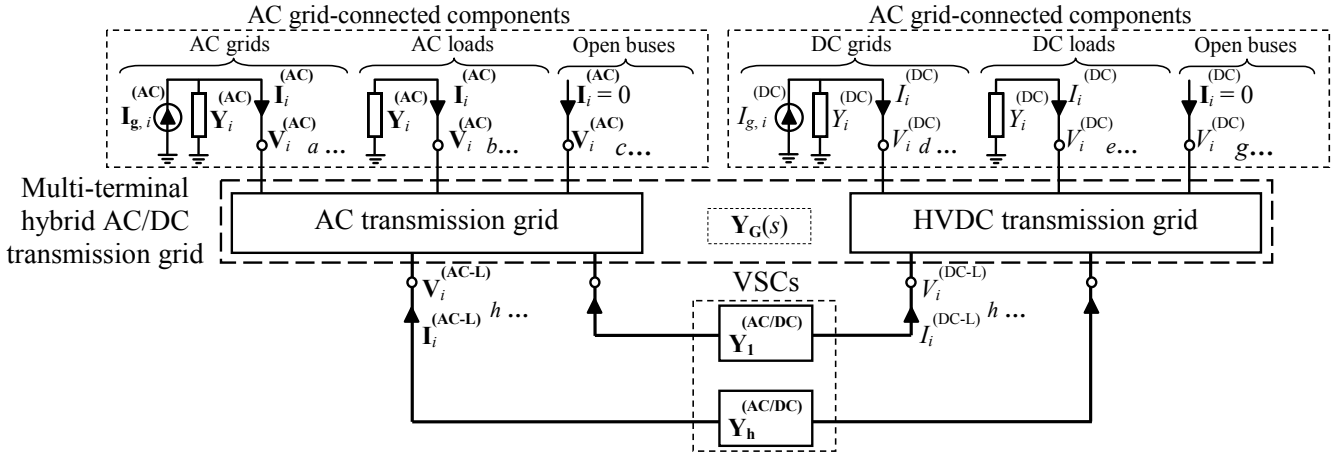


Fig. 5. Schematic diagram of multi-terminal HVDC hybrid AC/DC transmission grids.

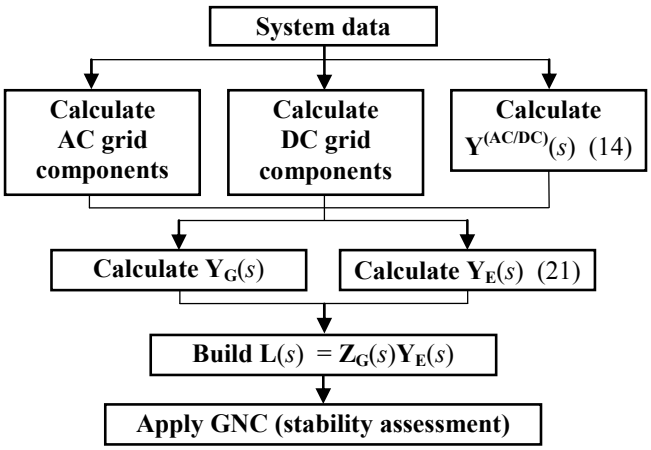


Fig. 6. Flowchart of the procedure.

$$\mathbf{v} = \begin{bmatrix} \left[\mathbf{V}^{(\mathbf{AC})}_{i=1,\ldots a+b+c}\right]_{2x1} \\ V^{(DC)}_{i=1,\ldots d+e+g} \\ \left[\mathbf{V}^{(\mathbf{AC/DC\text{-}L})}_{i=1,\ldots h}\right]_{3x1} \end{bmatrix} \qquad \mathbf{i_E} = \begin{bmatrix} \left[\mathbf{I}^{(\mathbf{AC})}_{g,i=1,\ldots a}\right]_{2x1} \\ \left[\mathbf{0}_{i=1,\ldots b+c}\right]_{2x1} \\ I^{(DC)}_{g,i=1,\ldots d} \\ 0_{i=1,\ldots e+g} \\ \left[\mathbf{0}_{i=1,\ldots h}\right]_{3x1} \end{bmatrix} \tag{21}$$

$$\mathbf{Y_E}(s) = \begin{bmatrix} \left[\mathbf{Y}^{(\mathbf{AC})}_{i=1,\ldots a+b+c}\right]_{2x2} & \cdots & 0 \\ \vdots & Y^{(DC)}_{i=1,\ldots d+e+g} & \vdots \\ 0 & \cdots & \left[\mathbf{Y}^{(\mathbf{AC/DC})}_{i=1,\ldots h}\right]_{3x3} \end{bmatrix},$$

where the voltage vector at the VSC terminals is

$$\mathbf{V}_i^{(\mathbf{AC/DC\text{-}L})} = \begin{bmatrix} V_i^{(DC-L)} \\ \left[\mathbf{V}_i^{(\mathbf{AC\text{-}L})}\right]_{2x1} \end{bmatrix}. \tag{22}$$

Stability can be analyzed in frequency domain by rewriting (20) as,

$$\mathbf{v} = \left(\mathbf{I} + \mathbf{Z_G}(s)\mathbf{Y_E}(s)\right)^{-1} \mathbf{Z_G}(s)\mathbf{i_E}, \tag{23}$$

where $\mathbf{I}$ is the identity matrix and $\mathbf{Z_G}(s) = \mathbf{Y_G}^{-1}(s)$ is the grid impedance matrix. Stability of the closed loop system in (23) is assessed by the GNC, which extends the traditional Nyquist criterion to the Nyquist curves of the eigenvalues of the loop transfer function $\mathbf{L}(s) = \mathbf{Z_G}(s)\mathbf{Y_E}(s)$ [12], [18]. Although the absence of RHP poles in the loop transfer functions is a special case, the proposed approach ensures that $\mathbf{L}(s)$ does not have any RHP poles because the multi-terminal HVDC hybrid AC/DC transmission grid $\mathbf{Z_G}(s)$ is passive and the external components in the diagonal of $\mathbf{Y_E}(s)$ are individual subsystems without any interaction with other grid components (i.e., $\mathbf{Z_G}(s)$ and $\mathbf{Y_E}(s)$ do not have any RHP poles) [14]. Therefore, system stability can be assessed by encirclements of the eigenvalues of $\mathbf{L}(s)$ around the –1 point.

Fig. 6 shows the flowchart of the systematic procedure proposed for stability assessment.

## IV. Application

Stability problems in the multi-terminal AC/DC grid of Fig. 7(a) are analyzed to show the paper's contribution. The 110 kV 50 Hz main AC grid supplies two 1000 MW 220 kV HVDC transmission grids through two step-up 110/220 kV transformers and two VSCs operating in mode $V_{dc} - Q$ at unity power factor, which is common in normal operation conditions [9], [10]. The HVDC transmission grids connect the main AC grid with two AC grids through the DC cables and the $VSC_3$ and $VSC_4$, which operate in mode $P - Q$. $VSC_1$ and $VSC_2$ are characterized by their three-port small signal admittance matrices (14) while $VSC_3$ and $VSC_4$ are considered as constant power consumption $P_{20}$ and $P_{30}$ characterized by the fictive resistance $R_{i0} = -(V_{dci,\,0})^2/P_{i0}$ ($i$ = 2, 3), which consumes a current $\Delta V_{dci}/R_{i0}$ under the small

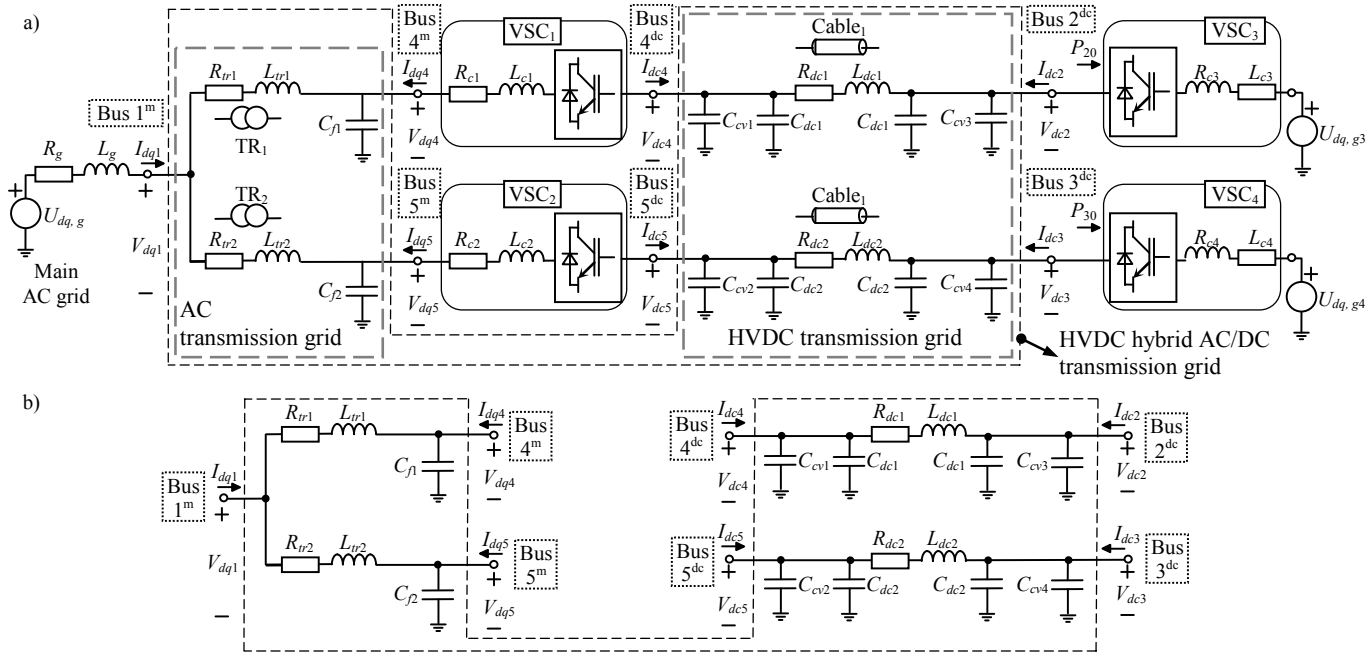


Fig. 7. Application: a) Multi-terminal HVDC hybrid AC/DC transmission system. b) HVDC hybrid AC/DC transmission grid.

signal voltage $\Delta V_{dci}$ [11]. These converters could also be modeled with their three-port small signal admittance matrices, but a simpler model is used in the stability study for the sake of simplicity. The AC grid is chosen as the *dq*-global reference frame of the multi-terminal HVDC hybrid AC/DC transmission grid. $VSC_1$ and $VSC_2$ have the same data as in Table I and the multi-terminal AC/DC grid data are in Table II. In order to study stability, the relations between voltages and currents at the multi-terminal HVDC hybrid AC/DC transmission grid are expressed as (23) where

- Impedance matrix of the HVDC hybrid AC/DC transmission grid in Fig. 7(b),

$$\begin{array}{l}\text{Bus \#}\quad 1^{\text{m}}\quad 2^{\text{dc}}\quad 3^{\text{dc}}\quad 4^{\text{dc}}\quad 4^{\text{m}}\quad 5^{\text{dc}}\quad 5^{\text{m}}\\ \mathbf{Z_G}=\begin{bmatrix} \mathbf{Y_1^{\pm}} & 0_{2x1} & 0_{2x1} & 0_{2x1} & -\mathbf{Y_{14}^{\pm}} & 0_{2x1} & -\mathbf{Y_{15}^{\pm}} \\ 0_{1x2} & Y_2 & 0_{1x1} & -Y_{24} & 0_{1x2} & 0_{1x1} & 0_{1x2} \\ 0_{1x2} & 0_{1x1} & Y_3 & 0_{1x1} & 0_{1x2} & -Y_{35} & 0_{1x2} \\ 0_{1x2} & -Y_{24} & 0_{1x1} & Y_4 & 0_{1x2} & 0_{1x1} & 0_{1x2} \\ -\mathbf{Y_{14}^{\pm}} & 0_{2x1} & 0_{2x1} & 0_{2x1} & \mathbf{Y_4^{\pm}} & 0_{2x1} & 0_{2x2} \\ 0_{1x2} & 0_{1x1} & -Y_{35} & 0_{1x1} & 0_{1x2} & Y_5 & 0_{1x2} \\ -\mathbf{Y_{15}^{\pm}} & 0_{2x1} & 0_{2x1} & 0_{2x1} & 0_{2x2} & 0_{2x1} & \mathbf{Y_5^{\pm}} \end{bmatrix}^{-1}\end{array}, \quad (24)$$

where

$$\begin{aligned} &\mathbf{Y_1^{\pm}}=(\mathbf{Z_{tr1}^{\pm}})^{-1}+(\mathbf{Z_{tr2}^{\pm}})^{-1} \qquad \mathbf{Y_4^{\pm}}=(\mathbf{Z_{tr1}^{\pm}})^{-1}+(\mathbf{Z_{f1}^{\pm}})^{-1} \\ &\mathbf{Y_5^{\pm}}=(\mathbf{Z_{tr2}^{\pm}})^{-1}+(\mathbf{Z_{f2}^{\pm}})^{-1} \quad \mathbf{Y_{14}^{\pm}}=(\mathbf{Z_{tr1}^{\pm}})^{-1} \quad \mathbf{Y_{15}^{\pm}}=(\mathbf{Z_{tr2}^{\pm}})^{-1} \\ &Y_2=C_{cv3}s+C_{dc1}s+(R_{dc1}+L_{dc1}s)^{-1} \\ &Y_3=C_{cv4}s+C_{dc2}s+(R_{dc2}+L_{dc2}s)^{-1} \\ &Y_4=C_{cv1}s+C_{dc1}s+(R_{dc1}+L_{dc1}s)^{-1} \\ &Y_5=C_{cv2}s+C_{dc2}s+(R_{dc2}+L_{dc2}s)^{-1} \\ &Y_{24}=(R_{dc1}+L_{dc1}s)^{-1} \qquad Y_{35}=(R_{dc2}+L_{dc2}s)^{-1}, \end{aligned} \quad (25)$$

and

$$\begin{aligned} &\mathbf{Z_{tr}^{\pm}}_i=\begin{bmatrix} \mathbf{Z_{tr}^{+}}_i & \mathbf{Z_{tr}^{-}}_i \\ (\mathbf{Z_{tr}^{-}}_i)^{*} & (\mathbf{Z_{tr}^{+}}_i)^{*} \end{bmatrix} \qquad \mathbf{Z_{fi}^{\pm}}=\begin{bmatrix} \mathbf{Z_{fi}^{+}} & \mathbf{Z_{fi}^{-}} \\ (\mathbf{Z_{fi}^{-}})^{*} & (\mathbf{Z_{fi}^{+}})^{*} \end{bmatrix} \\ &\mathbf{Z_{tri}^{+}}=R_{tri}+L_{tri}(s+j\omega_1) \qquad \mathbf{Z_{tri}^{-}}=0 \\ &\mathbf{Z_{fi}^{+}}=\left(C_{fi}(s+j\omega_1)+\frac{R_{fi}+L_{fi}(s+j\omega_1)}{R_{fi}L_{fi}(s+j\omega_1)}\right)^{-1} \qquad \mathbf{Z_{fi}^{-}}=0. \end{aligned} \quad (26)$$

- Admittance matrix of the external components,

$$\begin{array}{l}\text{Bus \#}\quad 1^{\text{m}}\quad 2^{\text{dc}}\quad 3^{\text{dc}}\quad 4^{\text{dc-m}}\quad 5^{\text{dc-m}}\\ \mathbf{Y_E}=\begin{bmatrix} \mathbf{Y_g^{\pm}} & 0_{2x1} & 0_{2x1} & 0_{2x3} & 0_{2x3} \\ 0_{1x2} & R_{20}^{-1} & 0_{1x1} & 0_{1x3} & 0_{1x3} \\ 0_{1x2} & 0_{1x1} & R_{30}^{-1} & 0_{1x3} & 0_{1x3} \\ 0_{3x2} & 0_{3x1} & 0_{3x1} & \mathbf{Y_4^{(AC/DC)}} & 0_{3x3} \\ 0_{3x2} & 0_{3x1} & 0_{3x1} & 0_{3x3} & \mathbf{Y_5^{(AC/DC)}} \end{bmatrix}\begin{array}{l} 1^{\text{m}} \\ 2^{\text{dc}} \\ 3^{\text{dc}} \\ 4^{\text{dc-m}} \\ 5^{\text{dc-m}} \end{array}\\ \text{Bus \#}\end{array}, \quad (27)$$

TABLE II
HYBRID AC/DC TRANSMISSION GRID DATA
BASE VALUES: $U_{B,\text{AC}}$ = 220 kV, $U_{B,\text{DC}}$ = 440 kV, $S_B$ = 1000 MVA

| | Parameters | Data |
|---|---|---|
| AC Main grid | $U_0$ ($f_1$) | 110 kV (50 Hz) |
| | $SCR = S_{cc}/(2\cdot P_{vsci,\text{N}})$ | 20 pu |
| | $X_g/R_g$ | 20 pu |
| Transformers ($i$ = 1, 2) | $S_{Ni}$, $U_{N1,i}/U_{N2,i}$ | 1000 MVA, 110/220 kV |
| | $\varepsilon_{cci}$, $X_{tri}/R_{tri}$ | 2.5 %, 20 pu |
| VSC AC filters | $C_{fi}$ ($i$ = 1, 2) | 20 μF |
| VSC DC filters | $C_{cvi}$ ($i$ = 1 to 4) | 30 μF |
| DC cables ($i$ = 1, 2) | $R_{dci}$, $L_{dci}$ | 10.8 mΩ/km, 0.149 mH/km |
| | $C_{dci}$, Length | 0.145 μF/km, 25 km |

where $\mathbf{Y_4^{(AC/DC)}}$ and $\mathbf{Y_5^{(AC/DC)}}$ are the $VSC_1$ and $VSC_2$ three-port small signal admittance matrices (14) and

$$\begin{aligned} &\mathbf{Y_g^{\pm}}=\begin{bmatrix} \mathbf{Z_g^{+}} & \mathbf{Z_g^{-}} \\ (\mathbf{Z_g^{-}})^{*} & (\mathbf{Z_g^{+}})^{*} \end{bmatrix}^{-1} \qquad \mathbf{Z_g^{-}}=0 \\ &\mathbf{Z_g^{+}}=R_g+L_g(s+j\omega_1) \qquad (\mathbf{Z_g^{+}})^{*}=R_g+L_g(s-j\omega_1). \end{aligned} \quad (28)$$

The example studies four cases:

- Case #1: this is the stable reference case, which corresponds to the steady-state operating point with data in Tables I and II, and with the power consumed by $VSC_3$ and $VSC_4$ being half the nominal power (i.e., $P_{i0}$ = 500 MW $i$ = 2, 3).
- Case #2: the influence of VSC filter capacitors $C_{f1}$ and $C_{f2}$ on system harmonic stability is analyzed. Stability of the steady-state operating point of Case #1 with $C_{f1} = C_{f2}$ = 10 μF is assessed.
- Case #3: the influence of the $VSC_3$ and $VSC_4$ consumed powers on system harmonic stability is analyzed. Stability of the steady-state operating point of Case #1 with $P_{20} = P_{30}$ = 1000 MW is assessed.
- Case #4: the influence of the short-circuit ratio (*SCR*) on system subsynchronous stability is analyzed. Stability of the steady-state operating point of Case #1 with *SCR* = 1 pu is assessed.

Small signal system stability around the previous steady-state operating points is investigated from the GNC of the loop transfer function $\mathbf{L}(s) = \mathbf{Z_G}(s)\mathbf{Y_E}(s)$ and PSCAD/EMTDC time-domain simulations. In these simulations, the variables of the AC/DC transmission grid of $VSC_1$ and $VSC_3$ are only shown because the results are the same for the variables of the AC/DC transmission grid of $VSC_2$ and $VSC_4$ due to the symmetry of the circuit.

In Case #1, the GNC verifies system stability because the curves of the eigenvalues of $\mathbf{L}(s)$ in Fig. 8 do not encircle the −1 point (for the sake of clarity, only the curves of eigenvalues related to system instability are plotted). In this steady-state operating point, the resonance frequencies of the system are damped by the system resistances.

In Case #2, the value of the filter capacitors $C_{f1}$ and $C_{f2}$ is reduced from 20 μF to 10 μF at 0.4 s. According to the PSCAD/EMTDC simulations in Fig. 9(a), the system becomes

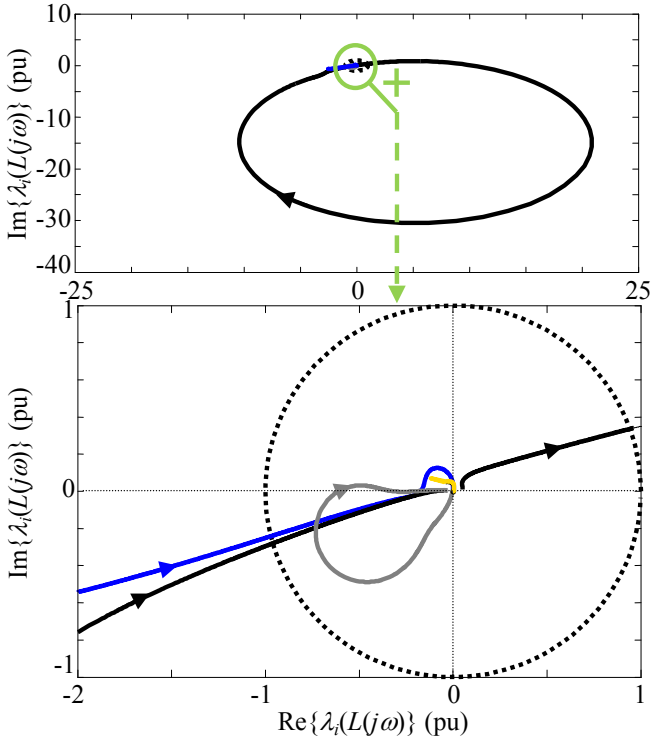


Fig. 8. Stability study: Case #1.

unstable after the capacitor value ramp down. This is because the frequencies of the system resonances are shifted and the resonance at $f \approx 820$ Hz (i.e., the frequency of the unstable harmonic oscillations captured in the frequency spectrum in Fig. 9(a)) is in the VSC negative-damping region which is not compensated by the system resistances. This VSC negative-damping region is mainly affected by the grid voltage feedforward low-pass filter bandwidth and VSC time delay, which could be modified to achieve VSC passivity at this frequency. The GNC verifies the instability results because the curves of one eigenvalue intersect the unit circle approximately at 813 Hz, enclosing the −1 point in clockwise direction, Fig. 10(a). The frequency of the intersection points is verified in the Bode plot of this eigenvalue (middle and bottom plots in Fig. 10(a)).

In Case #3, the $VSC_3$ and $VSC_4$ consumed active powers are raised from 500 MW ($P_{20} = P_{30} = 500$ MW) to the nominal value ($P_{20} = P_{30} = 1000$ MW) at 0.1 s. According to the PSCAD/EMTDC simulations in Fig. 9(b), the system becomes unstable after the active power consumptions are ramp up. This is because the value of the fictive resistance $R_{30}$ is modified and the DC resonance at $f \approx 630$ Hz (i.e., the frequency of the unstable harmonic oscillations captured in the frequency spectrum in Fig. 9(b)) is not damped by the system resistances. The GNC verifies the instability results because the curve of two eigenvalues intersects the unit circle approximately at 638 and 641 Hz, enclosing the −1 point in clockwise direction, Fig. 10(b). The frequency of the intersection point is verified in the Bode plot of these eigenvalues (middle and bottom plots in Fig. 10(b)).

In Case #4, the short-circuit ratio *SCR* is reduced from 20 pu to 1 pu at 0.3 s (i.e., $VSC_1$ and $VSC_2$ are connected to a very weak AC grid at 0.3 s). According to the

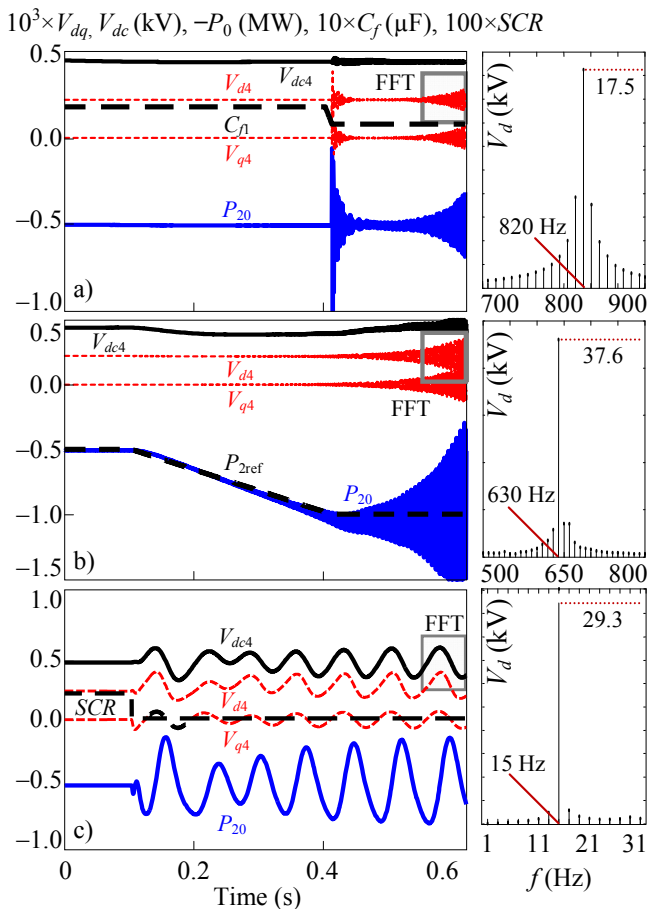


Fig. 9. PSCAD simulations (time-domain waveforms on the left and frequency spectrum on the right): a) Case #2. b) Case #3. c) Case #4.

PSCAD/EMTDC simulations in Fig. 9(c), the system becomes unstable after the *SCR* value is stepped down. This is because the weak AC grid shifts the system resonance to the subsynchronous frequency $f \approx 15$ Hz (i.e., the frequency of the unstable subsynchronous oscillations captured in the frequency spectrum in Fig. 9(c)), where the VSCs have a negative resistance due to the PLL and the outer loops. A small grid voltage feedforward low-pass filter bandwidth could be used to keep as narrow as possible the VSC non-passivity region caused by outer control loops at near-synchronous frequencies [4], [9]. The GNC verifies the instability results because the curve of one eigenvalue intersects the unit circle approximately at 15.2 Hz, enclosing the −1 point in clockwise direction, Fig. 10(c). The frequency of the intersection point is verified in the Bode plot of this eigenvalue (middle and bottom plots in Fig. 10(c)).

## V. Conclusions

The paper presents two contributions to the study of multi-terminal HVDC hybrid AC/DC transmission grid stability: (i) a new VSC three-port admittance-based model, which extends the VSC models in the literature, and (ii) a systematic procedure based on the Norton admittance method for modeling these grids. The proposed model characterizes both the AC- and DC-side dynamics by relating the AC- and DC-side currents and voltages from a three-port admittance

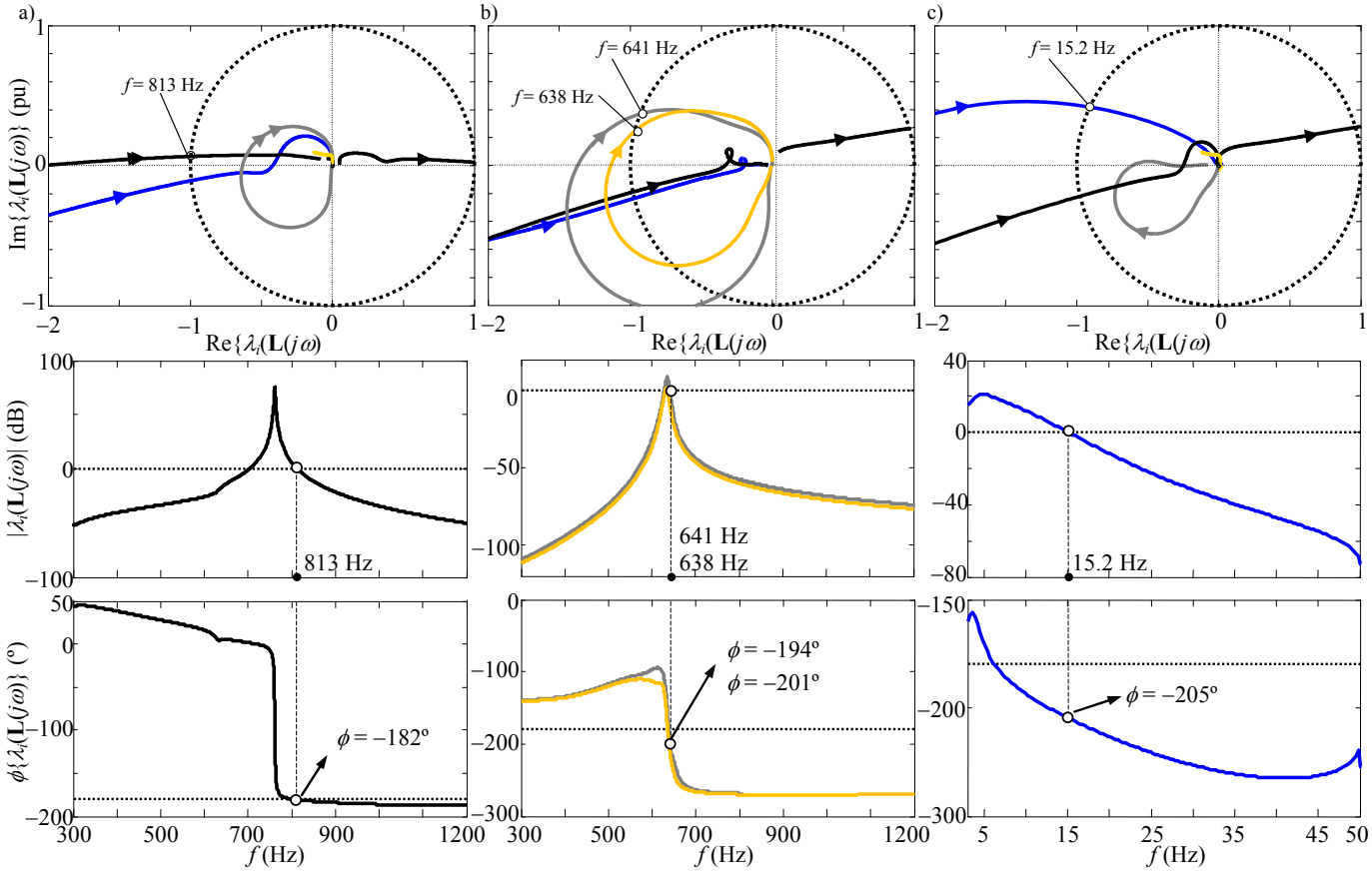


Fig. 10. Stability study: a) Case #2. b) Case #3. c) Case #4.

transfer matrix (one port for the DC-side and two *dq*-complex ports for the AC-side) independent of the AC and DC grids connected to these ports. The proposed procedure is rigorous, understandable and easy to program and can be used to analyze multi-terminal HVDC hybrid AC/DC transmission grid stability using impedance-based stability criteria. Both contributions are shown in a multi-terminal HVDC hybrid AC/DC transmission grid application.

## APPENDIX

### A. Complex Transfer Functions

Complex transfer functions are used in Section II to model grid-connected VSC systems with *dq*-complex space vectors [14], [16], [17].

A *dq*-domain impedance matrix of *dq*-real space vectors,

$$\begin{bmatrix} U_d \\ U_q \end{bmatrix} = \begin{bmatrix} Z_{dd}(s) & Z_{dq}(s) \\ Z_{qd}(s) & Z_{qq}(s) \end{bmatrix} \begin{bmatrix} I_d \\ I_q \end{bmatrix}, \tag{29}$$

can be transformed into another *dq*-frame matrix based on *dq*-complex space vectors as [16], [17], [19]

$$\begin{bmatrix} \mathbf{U_{dq}} \\ \mathbf{U_{dq}^*} \end{bmatrix} = \frac{1}{\sqrt{2}} \begin{bmatrix} 1 & j \\ 1 & -j \end{bmatrix} \begin{bmatrix} Z_{dd}(s) & Z_{dq}(s) \\ Z_{qd}(s) & Z_{qq}(s) \end{bmatrix} \frac{1}{\sqrt{2}} \begin{bmatrix} 1 & 1 \\ -j & j \end{bmatrix} \begin{bmatrix} \mathbf{I_{dq}} \\ \mathbf{I_{dq}^*} \end{bmatrix}$$
$$\Rightarrow \underbrace{\begin{bmatrix} \mathbf{U_{dq}} \\ \mathbf{U_{dq}^*} \end{bmatrix}}_{\mathbf{U_{dq}^m}} = \underbrace{\begin{bmatrix} \mathbf{Z}^+(s) & \mathbf{Z}^-(s) \\ (\mathbf{Z}^-(s))^* & (\mathbf{Z}^+(s))^* \end{bmatrix}}_{\mathbf{Z}^{\pm}(s)} \underbrace{\begin{bmatrix} \mathbf{I_{dq}} \\ \mathbf{I_{dq}^*} \end{bmatrix}}_{\mathbf{I_{dq}^m}}, \tag{30}$$

where

$$\mathbf{Z}^+(s) = \frac{Z_{dd}(s) + Z_{qq}(s)}{2} + j\frac{Z_{qd}(s) - Z_{dq}(s)}{2}$$
$$\mathbf{Z}^-(s) = \frac{Z_{dd}(s) - Z_{qq}(s)}{2} + j\frac{Z_{qd}(s) + Z_{dq}(s)}{2}. \tag{31}$$

The *dq*-complex space vectors are defined as $\mathbf{U_{dq}} = (U_d + jU_q)/\sqrt{2}$ and $\mathbf{I_{dq}} = (I_d + jI_q)/\sqrt{2}$. Transformation (31) is also true for any *dq*-domain matrix of *dq*-real space vectors, e. g., admittance matrices.

### B. VSC Modeling

The *dq*-real small signal impedance-based model of the VSC in Fig. 1 is briefly reviewed in this Section [9], [10], [12]. The VSC control is characterized by the inner current controller (CC) and the outer control loops, which make it possible to characterize the main VSC operation modes (i.e., mode $P - Q$, mode $V_{dc} - Q$, mode $V_{dc} - E_{ac}$ and mode $P - E_{ac}$) [9], [10]. The PLL is also considered in the control modeling and the superscript "c" indicates the converter *dq*-domain variables whereas no superscript is used on the grid *dq*-domain variables.

#### 1) AC grid relation

According to Fig. 1, the small signal voltage balance in grid *dq*-domain across the converter $R_c - L_c$ filter is

$$\begin{bmatrix}\Delta E_d\\ \Delta E_q\end{bmatrix}=\begin{bmatrix}R_c+sL_c & -L_c\omega_1\\ L_c\omega_1 & R_c+sL_c\end{bmatrix}\begin{bmatrix}\Delta I_d\\ \Delta I_q\end{bmatrix}+\begin{bmatrix}\Delta V_d\\ \Delta V_q\end{bmatrix}, \quad (32)$$

where $\omega_1 = 2\pi f_1$ is the fundamental angular frequency of the grid, $V_{dq} = [V_d\ V_q]^T$ is the VSC output voltage and $E_{dq} = [E_d\ E_q]^T$ and $I_{dq} = [I_d\ I_q]^T$ are the voltage and the current at the point of common coupling.

*2) AC-DC converter relations*

The modulation function $m_{dq} = [m_d\ m_q]^T$ is used to relate the VSC output voltage $V_{dq}$ and the DC voltage $V_{dc}$ as [12]

$$\begin{bmatrix}V_d\\ V_q\end{bmatrix}=\begin{bmatrix}m_d\\ m_q\end{bmatrix}V_{dc} \quad\Rightarrow\quad \begin{bmatrix}\Delta V_d\\ \Delta V_q\end{bmatrix}=\begin{bmatrix}\Delta m_d\\ \Delta m_q\end{bmatrix}V_{dc0}+\begin{bmatrix}m_{d0}\\ m_{q0}\end{bmatrix}\Delta V_{dc}, \quad (33)$$

where $V_{dc0}$ and $m_{dq0}$ are the steady-state operating points of the DC voltage and the modulation function, respectively.

Assuming a lossless VSC and disregarding the homopolar component, the instantaneous power balance between the AC and DC sides of the VSC in Fig. 1 and (33) impose the following relation between the DC current $I_{dc}$ and the AC current [12]:

$$P_{dc}=P_{ac} \quad\Rightarrow\quad V_{dc}I_{dc}=-\begin{bmatrix}m_d & m_q\end{bmatrix}V_{dc}\begin{bmatrix}I_d\\ I_q\end{bmatrix}, \quad (34)$$

which can be expressed as the small signal relation,

$$\begin{aligned}&\Delta I_{dc}=-\begin{bmatrix}m_{d0} & m_{q0}\end{bmatrix}\begin{bmatrix}\Delta I_d\\ \Delta I_q\end{bmatrix}-\begin{bmatrix}I_{d0} & I_{q0}\end{bmatrix}\begin{bmatrix}\Delta m_d\\ \Delta m_q\end{bmatrix}\\ &\Rightarrow\quad \Delta I_{dc}=-m_{dq0}^T\Delta I_{dq}-I_{dq0}^T\Delta m_{dq},\end{aligned} \quad (35)$$

where $I_{dq0}$ is the steady-state operating point of the AC current.

*3) PLL relations*

The AC current and voltage and the modulation function in the converter ($I^c_{dq}$, $E^c_{dq}$ and $m^c_{dq}$) and grid ($I_{dq}$, $E_{dq}$ and $m_{dq}$) *dq*-domains are related as [12]

$$\begin{aligned}&\begin{bmatrix}\Delta I_d^c\\ \Delta I_q^c\end{bmatrix}=\begin{bmatrix}\Delta I_d\\ \Delta I_q\end{bmatrix}+\begin{bmatrix}0 & G_{PLL}(s)I_{q0}\\ 0 & -G_{PLL}(s)I_{d0}\end{bmatrix}\begin{bmatrix}\Delta E_d\\ \Delta E_q\end{bmatrix}\\ &\begin{bmatrix}\Delta E_d^c\\ \Delta E_q^c\end{bmatrix}=\begin{bmatrix}1 & G_{PLL}(s)E_{q0}\\ 0 & 1-G_{PLL}(s)E_{d0}\end{bmatrix}\begin{bmatrix}\Delta E_d\\ \Delta E_q\end{bmatrix}\\ &\begin{bmatrix}\Delta m_d^c\\ \Delta m_q^c\end{bmatrix}=\begin{bmatrix}\Delta m_d\\ \Delta m_q\end{bmatrix}+\begin{bmatrix}0 & G_{PLL}(s)m_{q0}\\ 0 & -G_{PLL}(s)m_{d0}\end{bmatrix}\begin{bmatrix}\Delta E_d\\ \Delta E_q\end{bmatrix},\end{aligned} \quad (36)$$

where $G_{PLL}(s) = F_{PLL}(s)/(s+E_{d0}F_{PLL}(s))$, $F_{PLL}(s) = k_{p,\,PLL}+k_{i,\,PLL}/s$ and $k_{p,\,PLL}$ and $k_{i,\,PLL}$ are the proportional and integral gains of the PLL control.

*4) Inner CC loop relations*

The small signal control law of the inner CC loop in the converter *dq*-domain is [9], [12]

$$\begin{aligned}&\begin{bmatrix}\Delta V_{d,r}^c\\ \Delta V_{q,r}^c\end{bmatrix}=-D(s)\left\{\begin{bmatrix}F_{cc}(s) & 0\\ 0 & F_{cc}(s)\end{bmatrix}\begin{bmatrix}\Delta I_{d,r}^c-\Delta I_d^c\\ \Delta I_{q,r}^c-\Delta I_q^c\end{bmatrix}-\right.\\ &\left.\begin{bmatrix}0 & -L_c\omega_1\\ L_c\omega_1 & 0\end{bmatrix}\begin{bmatrix}\Delta I_d^c\\ \Delta I_q^c\end{bmatrix}+\begin{bmatrix}H_f(s) & 0\\ 0 & H_f(s)\end{bmatrix}\begin{bmatrix}\Delta E_d^c\\ \Delta E_q^c\end{bmatrix}\right\},\end{aligned} \quad (37)$$

where $V^c_{dq,\,r} = [V^c_{d,r}\ V_{q,r}]^T = V_{dc0}[m_d\ m_q]^T$ and $I^c_{dq,r} = [I^c_{d,r}\ I^c_{q,r}]^T$ are the reference voltage and current, $D(s) = e^{-sTd}$ is the VSC time delay transfer function, $F_{cc}(s) = k_{p,\,cc}+k_{i,\,cc}/s$ and $H_f(s) = \alpha_f/(s+\alpha_f)$, with $k_{p,\,cc}$ and $k_{i,\,cc}$ being the proportional and integral gains of the inner CC, $\alpha_f$ the low-pass filter bandwidth and $T_d$ the VSC time delay.

*5) Outer control loop relations*

According to Fig. 1, the following outer control loops are characterized in the VSC modeling [9], [10], [14]:

Direct-voltage control (DVC) loop: The control law of the DVC is considered as

$$I_{d,r}^c=F_{dc}(s)(V_{dc,r}-V_{dc}) \quad\Rightarrow\quad \begin{bmatrix}\Delta I_{d,r}^c\\ \Delta I_{q,r}^c\end{bmatrix}=-\begin{bmatrix}F_{dc}(s)\\ 0\end{bmatrix}\Delta V_{dc}, \quad (38)$$

which is expressed with *dq*-complex space vectors (30) as

$$\Delta\mathbf{I}^{\mathbf{cm}}_{\mathbf{dq,r}}=-\mathbf{F}^{\mathbf{m}}_{\mathbf{o,DVC}}\Delta V_{dc} \qquad \mathbf{F}^{\mathbf{m}}_{\mathbf{o,DVC}}=\frac{1}{\sqrt{2}}\begin{bmatrix}F_{dc}(s)\\ F_{dc}(s)\end{bmatrix}, \quad (39)$$

where $F_{dc}(s) = k_{p,\,dc}+k_{i,\,dc}/s$, with $k_{p,\,dc}$ and $k_{i,\,dc}$ being the proportional and integral gains of the DVC.

Alternating-power control (APC) loop: Since $E_{q0} = 0$, the control law of the APC is considered as

$$\begin{aligned}&I_{d,r}^c=F_p(s)(P_{ref}-(E_dI_d+E_qI_q)) \quad\overset{E_{q0}=0}{\Rightarrow}\\ &\begin{bmatrix}\Delta I_{d,r}^c\\ \Delta I_{q,r}^c\end{bmatrix}=-F_p(s)\begin{bmatrix}E_{d0} & 0\\ 0 & 0\end{bmatrix}\begin{bmatrix}\Delta I_d\\ \Delta I_q\end{bmatrix}-F_p(s)\begin{bmatrix}I_{d0} & I_{q0}\\ 0 & 0\end{bmatrix}\begin{bmatrix}\Delta E_d\\ \Delta E_q\end{bmatrix},\end{aligned} \quad (40)$$

which is expressed with *dq*-complex space vectors (30) as

$$\begin{aligned}&\Delta\mathbf{I}^{\mathbf{cm}}_{\mathbf{dq,r}}=-\mathbf{G}^{\pm}_{\mathbf{o,APC}}\Delta\mathbf{I}^{\mathbf{cm}}_{\mathbf{dq}}-\mathbf{Y}^{\pm}_{\mathbf{o,APC}}\Delta\mathbf{E}^{\mathbf{cm}}_{\mathbf{dq}}\\ &\mathbf{G}^{\pm}_{\mathbf{o,APC}}=\frac{F_p(s)E_{d0}}{2}\begin{bmatrix}1 & 1\\ 1 & 1\end{bmatrix} \quad \mathbf{Y}^{\pm}_{\mathbf{o,APC}}=\frac{F_p(s)}{\sqrt{2}}\begin{bmatrix}\mathbf{I}^*_{\mathbf{dq0}} & \mathbf{I}_{\mathbf{dq0}}\\ \mathbf{I}^*_{\mathbf{dq0}} & \mathbf{I}_{\mathbf{dq0}}\end{bmatrix},\end{aligned} \quad (41)$$

where $F_p(s) = k_{p,\,p}+k_{i,\,p}/s$, with $k_{p,\,p}$ and $k_{i,\,p}$ being the proportional and integral gains of the APC.

Alternating-voltage control (AVC) loop: The control law of the DVC is considered as

$$\begin{aligned}&I_{q,r}^c=F_v(s)\left(E_{d,ref}-E_d\right) \quad\Rightarrow\\ &\begin{bmatrix}\Delta I_{d,r}^c\\ \Delta I_{q,r}^c\end{bmatrix}=-\begin{bmatrix}0 & 0\\ F_v(s) & 0\end{bmatrix}\begin{bmatrix}\Delta E_d\\ \Delta E_q\end{bmatrix},\end{aligned} \quad (42)$$

which is expressed with *dq*-complex space vectors (30) as

$$\Delta\mathbf{I}^{\mathbf{cm}}_{\mathbf{dq,r}} = -\mathbf{Y}^{\pm}_{\mathbf{o,AVC}}\Delta\mathbf{E}^{\mathbf{cm}}_{\mathbf{dq}} \qquad \mathbf{Y}^{\pm}_{\mathbf{o,AVC}} = \frac{F_v(s)}{2}\begin{bmatrix} j & j \\ -j & -j \end{bmatrix}, \quad (43)$$

where $F_v(s) = k_{p,v} + k_{i,v}/s$, with $k_{p,v}$ and $k_{i,v}$ being the proportional and integral gains of the AVC.

Reactive-power control (QPC) loop: Since $E_{q0} = 0$, the control law of the QPC is considered as

$$I^c_{q,r} = -F_q(s)(Q_{ref} - (E_q I_d - E_d I_q)) \overset{E_{q0}=0}{\Rightarrow}$$
$$\begin{bmatrix} \Delta I^c_{d,r} \\ \Delta I^c_{q,r} \end{bmatrix} = -F_q(s)\begin{bmatrix} 0 & 0 \\ 0 & E_{d0} \end{bmatrix}\begin{bmatrix} \Delta I_d \\ \Delta I_q \end{bmatrix} - F_q(s)\begin{bmatrix} 0 & 0 \\ I_{q0} & -I_{d0} \end{bmatrix}\begin{bmatrix} \Delta E_d \\ \Delta E_q \end{bmatrix}, \quad (44)$$

which is expressed with *dq*-complex space vectors (30) as

$$\Delta\mathbf{I}^{\mathbf{cm}}_{\mathbf{dq,r}} = -\mathbf{G}^{\pm}_{\mathbf{o,QPC}}\Delta\mathbf{I}^{\mathbf{cm}}_{\mathbf{dq}} - \mathbf{Y}^{\pm}_{\mathbf{o,QPC}}\Delta\mathbf{E}^{\mathbf{cm}}_{\mathbf{dq}}$$
$$\mathbf{G}^{\pm}_{\mathbf{o,QPC}} = \frac{F_q(s)E_{d0}}{2}\begin{bmatrix} 1 & -1 \\ -1 & 1 \end{bmatrix} \quad (45)$$
$$\mathbf{Y}^{\pm}_{\mathbf{o,QPC}} = \frac{F_q(s)}{\sqrt{2}}\begin{bmatrix} -\mathbf{I}^{*}_{\mathbf{dq0}} & \mathbf{I}_{\mathbf{dq0}} \\ \mathbf{I}^{*}_{\mathbf{dq0}} & -\mathbf{I}_{\mathbf{dq0}} \end{bmatrix},$$

where $F_q(s) = k_{p,q} + k_{i,q}/s$, with $k_{p,q}$ and $k_{i,q}$ being the proportional and integral gains of the QPC.

The complex transfer matrices $\mathbf{F}^{\mathbf{m}}_{\mathbf{o}}$, $\mathbf{G}^{\pm}_{\mathbf{o}}$ and $\mathbf{Y}^{\pm}_{\mathbf{o}}$ in (8) are the sum of the above complex transfer matrices depending on the VSC operation mode.

## REFERENCES


[1] N. Flourentzou, V. G. Agelidis, G. D. Demetriades, "VSC-Based HVDC Power Transmission Systems: An overview," *IEEE Trans. on Power Electronics*, vol. 24, no. 3, pp. 592-602, March 2009.

[2] J. Sun, M. Li, Z. Zhang, T. Xu, J. He, H. Wang, G. Li, "Renewable energy transmission by HVDC across the continent: System challenges and opportunities," *CSEE Journal of Power and Energy Systems*, vol. 3, no. 4, pp. 353–364, Dec. 2017.

[3] M. Raza, E. Prieto-Araujo, O. Gomis-Bellmunt, "Small-signal stability analysis of offshore AC network having multiple VSC-HVDC systems," *IEEE Trans. on Power Delivery*, vol. 33, no. 2, pp. 830-839, April 2018.

[4] L. P. Kunjumuhammed, B. C. Pal, C. Oates, K. J. Dyke, "Electrical oscillations in wind farm systems: Analysis and insight based on detailed modeling," *IEEE Trans. Sustainable Energy*, vol. 7, no. 1, pp.51-62, Jan. 2016.

[5] X. Wang, F. Blaabjerg, "Harmonic stability in power electronic based power systems: Concept, modeling, and analysis," *IEEE Trans. on Smart Grid,* vol. 10, no. 3, pp. 2858-2870, March 2018.

[6] M. Cespedes, J. Sun, "Impedance Modeling and Analysis of Grid-Connected Voltage-Source Converters," *IEEE Trans. on Power Electronics*, vol. 29, no. 3, pp. 1254-1261, March 2014.

[7] M. K. Bakhshizadeh *et al*., "Couplings in Phase Domain Impedance Modeling of Grid-Connected Converters," *IEEE Trans. Power Electronics*, vol. 31, no. 10, pp. 6792–6796, March 2016.

[8] B. Wen *et al*., "Small signal stability analysis of three-phase AC systems in the presence of constant power loads based on measurements d-q frame impedances," *IEEE Trans. on Power Electronics*, vol. 30, no. 10, pp. 5952-5963, Oct. 2015.

[9] L. Harnefors, M. Bongiorno, S. Lundberg, "Input-admittance calculation and shaping for controlled voltage-source converters," *IEEE Trans. on Industrial Electronics*, vol. 54, no. 6, pp. 3323-3334, Dec. 2007.

[10] K. M. Alawasa, Y. A. I. Mohamed, W. Xu, "Active mitigation of subsynchronous interactions between PWM voltage-source converters and power networks," *IEEE Trans. Power Electron.*, vol. 29, no. 1, pp. 121–134, Jan. 2014.

[11] G. Stamatiou, M. Bongiorno, "Stability Analysis of two-terminal VSC-HVDC systems using net-damping criterion," *IEEE Trans. on Power Delivery*, vol. 31, no. 4, pp. 1748-1756, Aug. 2016.

[12] M. Amin, M. Molinas, "Small-signal stability assessment of power electronics based power systems: A discussion of impedance- and eigenvalue-based methods," *IEEE Trans. on Industry Applications*, vol. 53, no. 3, pp. 5014-5030, Sept./Oct.. 2017.

[13] L. Xu, L. Fan, Z. Miao, "DC Impedance-model Based Resonance Analysis of a VSC-HVDC System," *IEEE Trans. on Power Delivery*, vol. 30, no. 3, pp. 1221-1230, Jun. 2015.

[14] C. Zhang, M. Molinas, A. Rygg, X. Cai, "Impedance-based analysis of interconnected power electronics systems: Impedance network modeling and comparative studies of stability criteria," *IEEE Journal of Emerging and Selected Topics in Power Electronics*, DOI: 10.1109/JESTPE.2019.2914560 (*on line*).

[15] H. Liu, X. Xie, W. Liu, "An oscillatory stability criterion based on the unified dq-frame impedance network model for power systems with high-penetration renewables," *IEEE Trans. on Power Syst*., vol. 33, no. 3, pp. 3472-3485, May 2018.

[16] L. Harnefors, "Modeling of Three-phase dynamic systems using complex transfer functions and transfer matrices," *IEEE Trans. on Industrial Electronics,* vol. 54, no. 4, pp. 2239-2248, Aug. 2007.

[17] X. Wang, L. Harnefors, F. Blaabjerg, "Unified impedance model of grid-connected voltage-source converters," *IEEE Trans. on Power Electronics*, vol. 33, no. 2, pp. 1775-1785, Feb.. 2018.

[18] S. Shah, L. Parsa, "Impedance modeling of three-phase voltage source converters in *dq*, sequence and phasor domains," *IEEE Trans. on Energy Conversion*, vol. 32, no. 3, pp. 1139-1150, Sept. 2017.

[19] A. Rygg, M. Molinas, C. Zhang, X. Cai, "A modified sequence-domain impedance definition and its equivalence to the dq-domain impedance definition for the stability analysis of AC power electronic systems," *IEEE Journal of Emerging and Selected Topics in Power Electronics*, vol. 4, no. 4, pp. 1383-1396, Dec. 2016.

[20] C. Zhang, X. Cai, M. Molinas, A. Rygg "On the impedance modeling and equivalence of AC/DC-side stability analysis of a grid-tied type-IV wind turbine system," *IEEE Trans. on Energy Conversion*, vol. 34, no. 2, pp. 1000-1009, June 2019.

[21] C. Zhang, X. Cai, A. Rygg, M. Molinas, "Sequence domain SISO equivalent models of a grid-tied voltage source converter system for small-signal stability analysis," *IEEE Trans. Energy Conversion*, vol. 33, no. 2, pp. 741–749, June 2018.

[22] G.C. Paap, "Symmetrical components in the time domain and their application to power network calculations," *IEEE Trans. Power Syst*., vol. 15, no. 2, pp. 522-528, May 2000.

[23] J. Lesenne, F. Notelet, G. Seguier, "Introduction a l'Electrotechnique Approfondie," Paris: Technique&Documentation, 1981.

[24] H. Liu, X. Xie, "Impedance Network Modeling and Quantitative Stability Analysis of Sub-/Super-Synchronous Oscillations for Large-Scale Wind Power Systems," *IEEE Access*, vol. 6, pp. 34431-34438, June 2018.

[25] E. Ebrahimzadeh, F. Blaabjerg, X. Wang, C. L. Bak, "Harmonic stability and resonance analysis in large PMSG-based wind power plants," *IEEE Trans. on Sustainable Energy*, vol. 9, no. 1, pp. 12-23, Jan. 2018.

[26] Y. Li *et al*., "*Stability Analysis and Location Optimization Method for Multi-converter Power Systems Based on Nodal Admittance Matrix*," *IEEE Journal of Emerging and Selected Topics in Power Electronics*, DOI: 10.1109/JESTPE.2019.2954560 (Early access), Nov. 2019.

[27] B. Wen *et al*., "Influence of Phase-Locked Loop on Input Admittance of Three-Phase Voltage-Source Converters," in Proc. *XXVIII Annual IEEE Applied Power Electronics Conference and Exposition (APEC)*, Long Beach, CA, USA, 2013, pp. 897-904.

[28] D. Lu, X. Wang, F. Blaabjerg, "Impedance-Based Analysis of DC-Link Voltage Dynamics in Voltage-Source Converters," *IEEE Trans. on Power Electronics*, vol. 34, no. 4, pp. 3973-3985, April 2019.

[29] Y. Liao, X. Wang, "Stationary-Frame Complex-Valued Frequency-Domain Modeling of Three-Phase Power Converters," *IEEE Journal of Emerging and Selected Topics in Power Electronics*, DOI: 10.1109/JESTPE.2019.2963004 (Early access), Dec. 2019.